

Covalent Organic Framework Decorated with Vanadium as a New Platform for Prins Reaction and Sulfide Oxidation

Harsh Vardhan,[†] Gaurav Verma,[†] Swetha Ramani,[†] Ayman Nafady,[‡] Abdullah M. Al-Enizi,[‡] Yanxiong Pan,[§] Zhongyu Yang,[§] Hui Yang,[†] and Shengqian Ma^{*,†}

[†]Department of Chemistry, University of South Florida, 4202 E. Fowler Avenue, Tampa, Florida 33620, United States

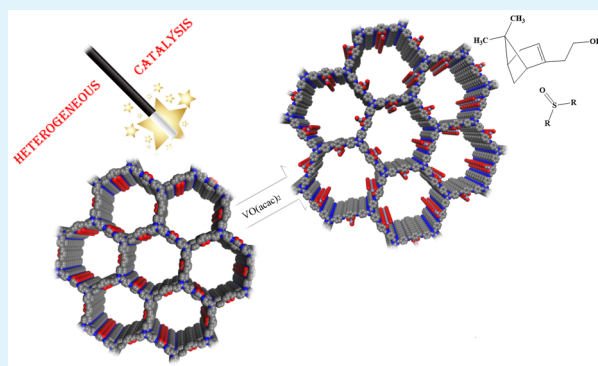
[‡]Department of Chemistry, College of Science, King Saud University, Riyadh 11451, Saudi Arabia

[§]Department of Chemistry and Biochemistry, North Dakota State University, 1231 Albrecht Blvd., Fargo, North Dakota 58108, United States

Supporting Information

ABSTRACT: Chemical functionalization or docking of transition-metal ions in covalent organic frameworks (COFs) is of importance for calibrating properties and widening potential applications. In this work, we demonstrate the successful decoration of COF with vanadium as exemplified in the context of post-synthetically modifying two-dimensional COF that features eclipsed stacking structure, large pores, hydroxyl functionalities, high thermal and chemical stability using vanadyl acetylacetonate. The potent catalytic behavior of vanadium-decorated COF was systematically investigated in the reactions of Prins condensation and sulfide oxidation, which revealed its excellent catalytic performances in terms of efficacious activity, preservation of framework crystallinity and reusability. Our work not only contributes the first ever report of vanadium-decorated COF-catalyzed Prins reaction and sulfide oxidation but paves a new way for docking COF with metals for a broad range of applications.

KEYWORDS: covalent organic frameworks, heterogeneous catalysis, Prins reaction, sulfide oxidation, postsynthetic modification



INTRODUCTION

Covalent organic frameworks (COFs), an emerging class of porous crystalline materials built by strong covalent bonds in a periodic arrangement of precursor units, have attracted a great deal of attention by virtue of low density (H, B, C, N, O), structural versatility, permanently high porosity, chemical and thermal stability.^{1–16} In last decade, considerable attention was focused on the design, synthesis and various applications such as gas storage and separation,^{17–22} catalysis,^{23–35} optoelectronics,^{36–38} environmental remediation,^{39,40} and so on.^{41–50} Two-dimensional (2D) and 3D COF structures were predominantly synthesized by boronic acid trimerization, trimerization of nitriles, Schiff-base formation, boronate ester trimerization, etc.^{7,12,13} From the catalysis viewpoint, the strong coordination between the organic linkers and transition-metal ions is a common way to impart active sites in catalyst. Group 5 elements especially vanadium and other high-valent transition-metal ions such as molybdenum are well known to form a range of complexes with bidentate O,O-donor and N,O-donor ligands of different symmetricity and point groups.^{51,52} Within this context, we judiciously choose 2,4,6-tris(4-aminophenyl)-1,3,5-triazine-2,3-dihydroxyterephthaldehyde (TAPT-2,3-DHTA) COF⁵³ bearing O,O functionalities

synthesized by the Schiff-base condensation reaction of 2,4,6-tris(4-aminophenyl)-1,3,5-triazine (TAPT) and 2,3-dihydroxyterephthaldehyde (2,3-DHTA) in presence of catalytic amount of 3 M acetic acid for vanadium immobilization. Intrigued by the stacked structure, high crystallinity, mesoporous channels, hydroxyl functionalities, chemical and thermal stability of TAPT-2,3-DHTA COF, we successfully immobilize vanadium functionalities to multiply the efficiency of modified framework in pivotal organic reactions underlining the fact that organic linkers are evenly distributed in porous material.

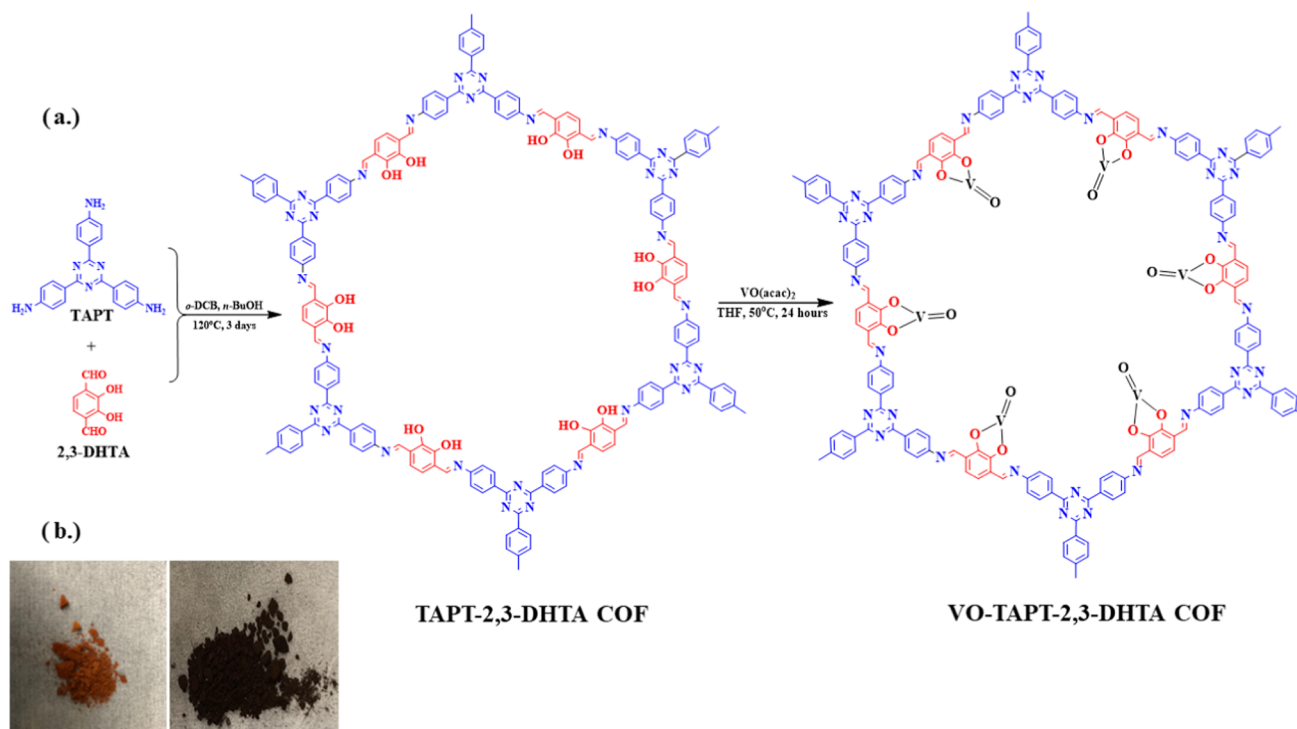
Prins-type cyclization is used to synthesize nopol, an important bicyclic primary alcohol used in agrochemical industry to form pesticide, detergents, perfumes, etc.^{54,55} Two most common ways to synthesize nopol in homogenous system are either by using ZnCl₂ at 115 °C or CH₃COOH at 120 °C followed by saponification of nopol acetate to nopol and reaction of paraformaldehyde and β-pinene in an autoclave at 150–230 °C.^{56,57} To avoid longer reaction time, higher

Received: November 4, 2018

Accepted: December 26, 2018

Published: December 26, 2018

Scheme 1. (a) Schematic Representations of 2D TAPT–2,3-DHTA COF and VO–TAPT–2,3-DHTA COF Synthesis; (b) Appearances of TAPT–2,3-DHTA COF (Left), VO–TAPT–2,3-DHTA COF (Right)



temperature and pressure and more importantly, opening the door for green synthetic routes, stable heterogeneous catalysts such as zeolites, metal–organic frameworks, MCM-41, Sn-SBA-15 are used for Prins reaction.^{58,59} In addition, the profound role of sulphoxide in chemical and medicinal industries makes the conversion of sulfide to sulphoxide in presence of oxidizing agent, an extremely important reaction.⁶⁰ Many oxidants such as MnO_2 , RuO_4 , NMO with OSO_4 and others are most common to perform this key transformation. Furthermore, homogenous organo-catalysts and polyoxometalates are widely used for sulfide oxidation;^{61,62} however, the role of porous materials especially COFs as heterogeneous catalyst is largely untapped for these pivotal reactions. In this contribution, we demonstrate the synthesis, characterization, and utilization of vanadium-docked COF, namely, VO–TAPT–2,3-DHTA as heterogeneous catalyst for Prins reaction and sulfide oxidation with excellent efficiency and reusability.

EXPERIMENTAL SECTION

Materials. All reagents and solvents were purchased from commercial sources and used without any further purification. 1,3,5-tris-(4-aminophenyl)triazine (TAPT)⁶³ and 2,3-dihydroxyterephthalaldehyde (2,3-DHTA),⁶⁴ $\text{K}_2[\text{VO}(\text{catechol})_2]$ ⁶⁵ were synthesized according to the previously reported procedure.

Synthesis of TAPT–2,3-DHTA COF. TAPT–2,3-DHTA COF was prepared as per the previously reported procedure.⁵³ A Pyrex tube measuring o.d. \times i.d. = $9.5 \times 7.5 \text{ mm}^2$ was charged with 2,3-dihydroxyterephthalaldehyde (7.5 mg, 0.045 mmol) and 1,3,5-tris-(4-aminophenyl) triazine (10.6 mg, 0.03 mmol) in 1.2 mL of a 5:5:2 v:v solution of *o*-dichlorobenzene/*n*-butanol/3 M aqueous acetic acid. The tube was flash-frozen at 77 K (liquid N_2 bath), evacuated, and flame-sealed. The reaction mixture was heated at 120 °C for 3 days to afford an orange precipitate, which was isolated by filtration and washed with dry tetrahydrofuran (THF) and dry acetone. The fluffy powder was dried at 120 °C under vacuum for 12 h before subjected to any characterization.

Synthesis of VO–TAPT–2,3-DHTA COF. To the 25 mL Schlenk tube, as-synthesized TAPT–2,3-DHTA COF (10 mg) was added into a solution of $\text{VO}(\text{acac})_2$ (61 mg) in THF (15 mL). The reaction mixture was heated at 50 °C in an oil bath under an inert atmosphere for 24 h. The precipitate so formed was centrifuged and washed with anhydrous THF and then with dry acetone to remove any excess metal ions. The product was dried under vacuum for 12 h before subjected to any characterization.

CATALYSIS

Prins Reaction. Typically, β -pinene (0.5 mmol), paraformaldehyde (1.0 mmol), and catalyst (50 mg) in CH_3CN were stirred at 80 °C for 12 h. Aliquots of the reaction mixture were sampled at different intervals and percentage yield was calculated using gas chromatography–mass spectrometry (GC–MS) analysis and mesitylene as an internal standard.

Sulfide Oxidation. Oxidation of sulfide to sulphoxide was carried out in a 10 mL Schlenk tube equipped with a magnetic bar. In a typical catalytic reaction, 1 mmol of sulfide, 1.5 mmol of *tert*-butyl hydroperoxide (TBHP), 20 mg of catalyst were mixed in 3 mL of CH_3CN . The reaction mixture was stirred at rt/40 °C, and on completion the mixture was subjected to GC–MS analysis using dodecane as an internal standard.

Characterization. ^1H NMR spectra measurements were done by using Varian Inova 400 MHz spectrometer. Powder X-ray diffraction (PXRD) data were collected at room temperature using Bruker D8 Advance X-ray diffractometer in a scanning range of 2–40°. Fourier transform infrared spectroscopy (FT-IR) measurements were done from 4000 to 400 cm^{-1} using Perkin Elmer Spectrometer with a resolution of 4 cm^{-1} . Thermal gravimetric analyses (TGA) were recorded from room temperature to 800 °C at 10 °C/min rate using TGA Q50. N_2 adsorption isotherm data at 77 K were collected using Micromeritics ASAP 2020 surface area analyzer, and CO_2 adsorption isotherms were measured at 298 K using water

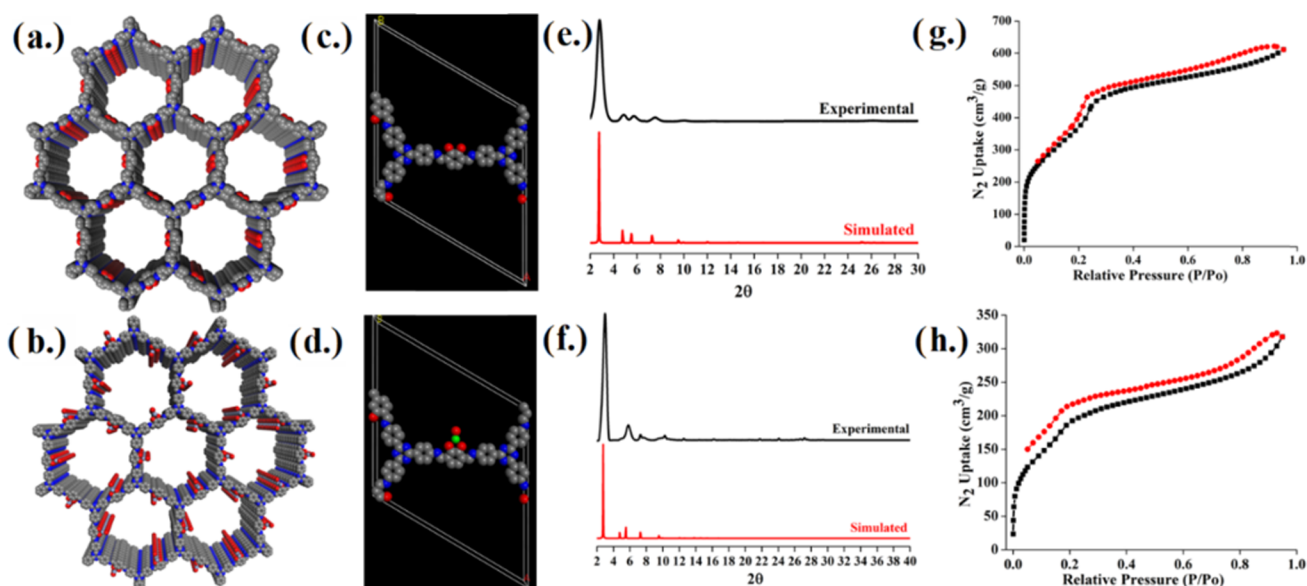


Figure 1. Graphic extended view of the stacking structure. (a) TAPT-2,3-DHTA COF; (b) VO-TAPT-2,3-DHTA COF. Unit cells of (c) TAPT-2,3-DHTA COF; (d) VO-TAPT-2,3-DHTA COF. Comparison of experimental and simulated PXRD pattern of (e) TAPT-2,3-DHTA COF; (f) VO-TAPT-2,3-DHTA COF. N_2 sorption isotherms of (g) TAPT-2,3-DHTA COF; (h) VO-TAPT-2,3-DHTA COF.

bath. The Brunauer–Emmett–Teller (BET) method was utilized to calculate the specific surface area. By using the nonlocal density functional theory model, the pore volume was derived from the sorption curve. Scanning electron microscopy (SEM) images were obtained with a Hitachi S 800 scanning electron microscope. X-ray photoelectron spectroscopic (XPS) analyses were carried out by using Perkin-Elmer PHI 5100 equipped with a Mg or Al nonmonochromatic X-ray. Variable temperature (PXRD) was collected at different temperatures using Rigaku SmartLab X-ray powder diffractometers. ^{13}C (100.5 MHz) cross polarization magic-angle spinning was recorded on a Varian infinity plus 400 spectrometer equipped with a magic-angle spin probe in a 4 mm ZrO_2 rotor. Elemental analyses were performed via flask combustion followed by ion chromatography. The crystalline structures of the COFs were constructed using Materials Studio, and the geometry and unit cell were optimized by the Forcite method. Universal force field and QuasiNewton algorithm were used for calculation. The XRD pattern simulations were performed in a software package for crystal determination from PXRD pattern, implemented in MS modeling. For electron paramagnetic resonance (EPR) measurement: “approximately 20 μL of powder was loaded into a borosilicate capillary tube (0.70 mm i.d./1.25 mm o.d.; VitroGlass, Inc.), which was mounted in a Varian E-109 spectrometer fitted with a cavity resonator. The continuous wave EPR spectrum was obtained with an observe power of 12.5 mW and a modulation amplitude of 10 G. The scan range is 2000 G, from 2500 to 4500 G. Signal average time is ~ 20 min”. Raman spectra were recorded on a confocal microscope-based Raman spectrometer (LabRam HR Evolution, Horiba Scientific). The excitation radiation is a He–Ne laser (633 nm), a diffraction grating of 600 l/m, and the spectral resolution was 1.8 cm^{-1} . Back-scattered photons passing through a 50 \times with 10.6 mm working distance and numerical aperture of 0.50 are filtered by a 633 nm edge filter before being detected by a Synapse back-illuminated deep depletion charge-coupled device (1024 \times 256 pixels).

RESULTS AND DISCUSSION

The orange-colored TAPT-2,3-DHTA COF containing bis-hydroxyl functionalities was fabricated as per the reported procedure⁵³ and completely characterized by means of physicochemical analysis (Figures S2–S6). Dark brown-colored vanadium-functionalized, VO-TAPT-2,3-DHTA, has been prepared by the single-step reaction of TAPT-2,3-DHTA with $\text{VO}(\text{acac})_2$ under inert atmosphere at 50 °C for 24 h, as shown in Scheme 1. The vanadium content of VO-TAPT-2,3-DHTA was measured to be 4.9 wt % by inductively coupled plasma mass spectrometry (ICP-MS). The successful grafting of vanadium moieties in TAPT-2,3-DHTA was confirmed by elemental analysis (Table S3), Fourier transform infrared spectroscopy (FT-IR), and other physicochemical analysis. The FT-IR signals at 1620, 1580, and 970 cm^{-1} are characteristic peaks of $\text{C}=\text{N}$, $\text{C}=\text{C}$, and $\text{V}=\text{O}$ stretching vibrations, respectively, suggested preservation of imine linkage in COF structure during postsynthetic modification (Figure S9). Powder X-ray diffraction (PXRD) pattern of pristine TAPT-2,3-DHTA displayed strong diffraction peak at 2.8° along with few weak peaks at 4.9, 5.9, 7.6, 10.1, 23.2° attributed to (100), (110), (200), (120), (220), and (001) facets, respectively, with $P1$ space group.

After vanadium grafting, the diffraction peaks remained comparable as naked TAPT-2,3-DHTA but with broadened weaker peaks (Figure 1). These broadened weak peaks ascribed to the incorporation of VO moieties in the pristine framework, furthermore, the simulated PXRD patterns of TAPT-2,3-DHTA and VO-TAPT-2,3-DHTA COFs match well with the experimental PXRD profile, thereby indicating that the structural crystallinity of COF has been well maintained during vanadium docking. This structural retention during different chemical or metal modifications in various 2D and 3D COFs was observed by various research groups including ours.^{39,66–68} Nitrogen sorption isotherm was measured to investigate the porous natures of TAPT-2,3-DHTA and VO-TAPT-2,3-DHTA COFs. Reversible type-IV isotherms were observed, which is typical for mesoporous

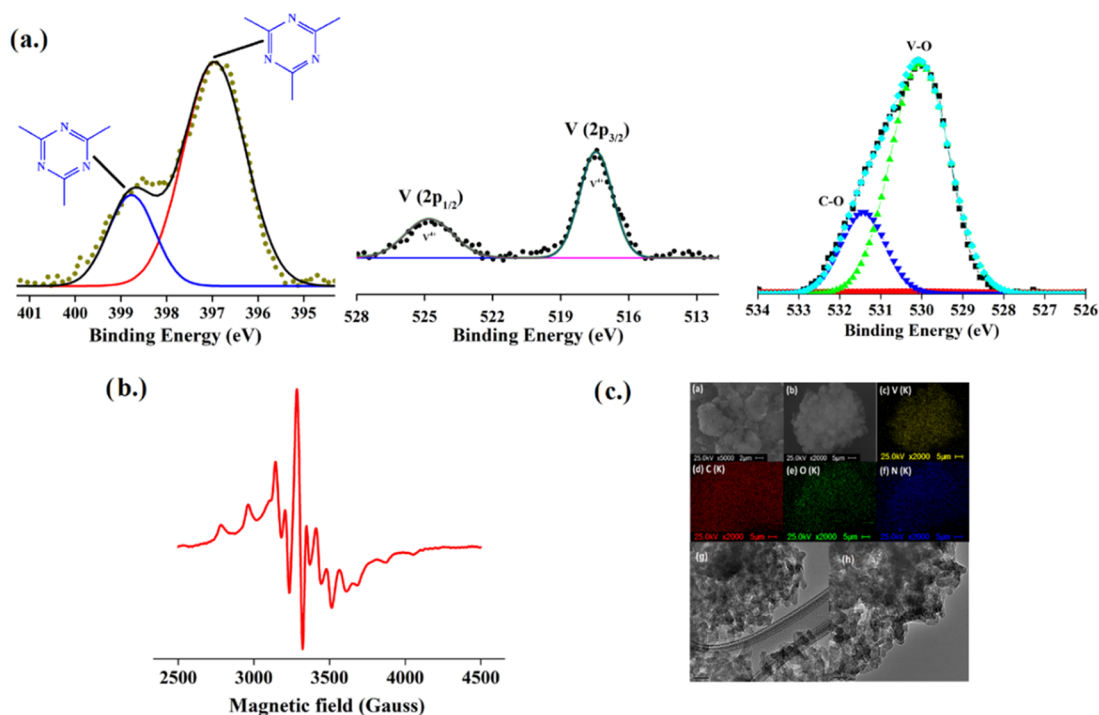


Figure 2. (a) XPS spectrum of VO-TAPT-2,3-DHTA COF; nitrogen (left), vanadium (middle), oxygen (right). (b) EPR spectrum of VO-TAPT-2,3-DHTA COF. (c) SEM images of (a) TAPT-2,3-DHTA COF, (b) VO-TAPT-2,3-DHTA COF and EDS mappings of (c) vanadium; (d) carbon; (e) oxygen; (f) nitrogen. TEM images of (g) TAPT-2,3-DHTA COF; (h) VO-TAPT-2,3-DHTA COF.

materials. As expected, the substantial decrease in the Brunauer–Emmett–Teller (BET), Langmuir surface area and pore size (nonlocal density functional theory) from 1151, 1490 m^2g^{-1} , 3.0 nm for TAPT-2,3-DHTA to 562, 750 m^2g^{-1} , 2.5 nm for VO-TAPT-2,3-DHTA was observed probably due to the partial immobilization of vanadium functionalities in pristine framework (Figures 1g–h and S7, S13). Even though, the pores of VO-TAPT-2,3-DHTA are partially occupied, the surface area is still high enough for ingress of substrates for catalytic reactions. Given the high thermal stability (up to 400 $^{\circ}\text{C}$) of VO-TAPT-2,3-DHTA, as shown by thermogravimetric analysis (TGA) (Figure S10), this class of vanadium-docked frameworks can be used as a potential heterogeneous catalyst at room or elevated temperature. Variable temperature PXRD pattern showed complete retention of all strong and weak peaks, as shown in Figure S11, further supporting the thermostability. ^{13}C NMR of VO-TAPT-2,3-DHTA showed carbon peaks of proposed structure, more importantly, the imine carbon at 169.9 ppm (Figure S15), thereby, indicating the retainment of imine functionalities during vanadium docking. We performed the Raman spectroscopy to further approve the vanadium docking, the additional peaks in Raman spectrum of VO-TAPT-2,3-DHTA COF at 1000–950 and 500–300 cm^{-1} regions in comparison to pristine TAPT-2,3-DHTA COF attributed to vanadyl group ($\text{V}=\text{O}$) and metal–oxygen ($\text{V}-\text{O}$) bonds confirmed the coordination between oxygen and vanadium species (Figure S16).⁶⁹ In general, the vibration frequency relies on ionic potential and covalent character of the bond under the sway of ligand field theory.

To understand the docking condition of vanadium in VO-TAPT-2,3-DHTA, X-ray photoelectron spectroscopy (XPS) was conducted. XPS spectra of TAPT-2,3-DHTA and VO-TAPT-2,3-DHTA COFs were analyzed. The N 1s spectra of VO-TAPT-2,3-DHTA showed two distinct peaks at 397 and

399 eV same as pristine TAPT-2,3-DHTA assigned to triazine units underlining the absence of any coordination with triazine nitrogen. Moreover, O 1s spectra showed an additional peak in comparison to pristine TAPT-2,3-DHTA at 529.8 eV assigned to the $\text{V}=\text{O}$ bond present in the modified framework. To identify the oxidation state of vanadium, the XPS spectra of V 2p region in VO-TAPT-2,3-DHTA highlighted the binding energies of V $2\text{p}_{1/2}$ and V $2\text{p}_{3/2}$ at 524 and 517 eV, respectively (Figure 2a), which in turn, indicated the presence of V(IV) in the modified framework. These results in totality indicated the strong interaction between the vanadium and oxygen in the modified framework. The presence of V^{4+} was further supported by electron paramagnetic resonance (EPR) analysis. The EPR spectrum of VO-TAPT-2,3-DHTA showed a characteristic of V(IV) with an axial pattern, as shown in Figure 2b. Maurya and co-workers reported similar observation for polymer-anchored vanadium complex.⁷⁰ The morphologies of both TAPT-2,3-DHTA and VO-TAPT-2,3-DHTA COFs were revealed by scanning electron microscopy (SEM) and transmission electron microscopy (TEM). As shown in Figure 2c, ribbon- or petal-like morphology was observed for parent and modified framework with a particle size of 410 nm (Figure S12), determined by dynamic light scattering (DLS). Energy-dispersive X-ray spectroscopy (EDS) via SEM showed the presence and even distribution of all the elements (C, N, O, V) in the modified framework, thereby implying a uniform postsynthetic modification, as shown in Figure 2c.

After determining the porosity, crystallinity, stability, and high density of VO-TAPT-2,3-DHTA, we characterize the catalytic performance in Prins reaction and sulfide oxidation. In doing so, the stability of VO-TAPT-2,3-DHTA in CH_3CN as a catalytic solvent was investigated using both PXRD and FT-IR (Figures S17 and S18). The percentage yield of nopol via

Prins condensation reaction of β -pinene (0.5 mmol) and paraformaldehyde (1.0 mmol) over TAPT-2,3-DHTA, VO(acac)₂, [VO(catechol)₂] at ambient or elevated (80 °C) temperature is negligible or moderate (<5, 19, and 21%), however, in presence of VO-TAPT-2,3-DHTA it increases to 69% (Table 1). This substantial increase in percentage yield

Table 1. Reaction Condition and Percentage Yield of Nopol Over TAPT-2,3-DHTA, VO-TAPT-2,3-DHTA COF, and Other Homogeneous Analogue^a

| entry | catalyst | A:B | temp (°C) | solvent | % yield |
|-------|---------------------------|-----|-----------|--------------------|---------|
| 1 | TAPT-2,3-DHTA | 1:2 | 25 | CH ₃ CN | <5 |
| 2 | TAPT-2,3-DHTA | 1:2 | 80 | CH ₃ CN | <5 |
| 3 | VO-TAPT-2,3-DHTA | 1:2 | 25 | CH ₃ CN | <10 |
| 4 | VO-TAPT-2,3-DHTA | 1:2 | 80 | CH ₃ CN | 69 |
| 5 | VO-TAPT-2,3-DHTA | 1:2 | 110 | toluene | 57 |
| 6 | VO(acac) ₂ | 1:2 | 80 | CH ₃ CN | 19 |
| 7 | VO(catechol) ₂ | 1:2 | 80 | CH ₃ CN | 21 |

^aReaction condition: β -pinene = 0.5 mmol; paraformaldehyde = 1.0 mmol; catalyst = 50 mg, containing 0.04 mmol of vanadium; CH₃CN = 3 mL; 100 rpm; 12 h; % yields were determined by GC-MS analysis.

ascribes to the mesoporous nature, large diameter of pore channel, and presence of active vanadium sites uniformly distributed in the framework. The use of CH₃CN, polar aprotic catalytic solvent in comparison to nonpolar solvent (toluene), positively affected the Prins condensation reaction by promoting better stabilization to the polar intermediate. GC mass spectrum of nopol is exactly similar to nopol NIST mass spectrum data base with characteristic *m/z* peaks at 105.1 and 91.1 (Figure S17). The catalytic efficiency comparison of VO-TAPT-2,3-DHTA with various other heterogeneous catalysts for nopol preparation is tabulated in Table S4. The plausible mechanism was proposed to explain the step-by-step conversion to nopol using VO-TAPT-2,3-DHTA. First, active vanadium sites are coordinated to oxygen of paraformaldehyde forming oxonium-like ion followed by electrophilic addition of β -pinene. Second, the carbocation undergoes concerted steps leading to the formation of nopol along with regeneration of catalyst, as shown in Figure 3.

In addition to nopol synthesis, we also attempted oxidation of aliphatic and aromatic sulfides in presence of 70% *tert*-butyl hydroperoxide (TBHP). The oxidation of thioanisole employed as a model reaction to study the catalytic behavior of VO-TAPT-2,3-DHTA in CH₃CN. Virtually, TAPT-2,3-DHTA showed poor catalytic performance, whereas VO-TAPT-2,3-DHTA and to some extent VO(catechol)₂, VO(acac)₂ exhibited excellent catalytic activity. The influences of reaction temperature and time on thioanisole oxidation are summarized in Table 2. The oxidation reaction at ambient temperature with varying stirring time 1, 2, 3, and 4 h showed corresponding sulphoxide selectivity 69, 82, 90, and 95%, albeit the same reaction at 40 °C revealed 89% sulphoxide selectivity within 2 h. The selectivity of sulfoxide decreased with increase in time due to the formation of sulfone as byproduct, and polar

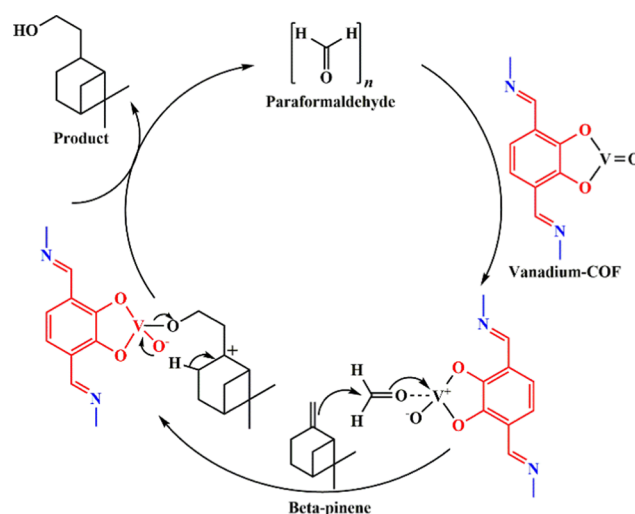


Figure 3. Plausible mechanism of Prins reaction catalyzed by VO-TAPT-2,3-DHTA COF.

Table 2. Oxidation of Thioanisole into Sulphoxide under Different Conditions^a

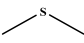
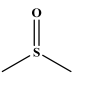
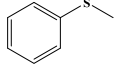
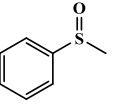
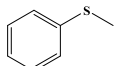
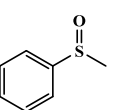
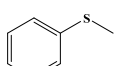
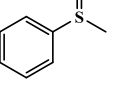
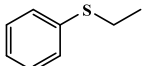
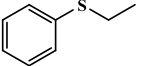
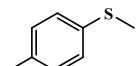
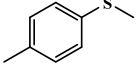
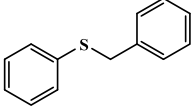
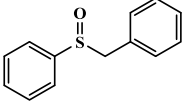
| entry | temp (°C) | time (h) | sulfide conversion (%) | sulphoxide selectivity (%) |
|-------|-----------|----------|------------------------|----------------------------|
| 1 | 25 | 1 | 61 | 69 |
| 2 | 25 | 2 | 76 | 82 |
| 3 | 25 | 3 | 93 | 90 |
| 4 | 25 | 4 | 99 | 95 |
| 5 | 40 | 2 | 99 | 89 |

^aReaction condition: thioanisole (1 mmol); *tert*-butyl hydroperoxide (TBHP) (1.5 mmol); catalyst (VO-TAPT-2,3-DHTA) = 20 mg, containing 0.019 mmol of vanadium; CH₃CN = 3 mL; 100 rpm.

aprotic solvent, CH₃CN, improve the stabilization of the intermediates. With the optimized condition, a range of sulfides under steric and electronic influences examined to illuminate the scope of VO-TAPT-2,3-DHTA as heterogeneous catalyst. It is noteworthy that this catalytic system withstands a range of electron-donating or -withdrawing substituents on aromatic ring and widely applicable, as shown in Table 3. The maximum sulfoxide percentage was observed for dimethyl sulfide, thioanisole, methyl *p*-tolyl sulfide, ethyl phenyl sulfide. However, the presence of bulky substitution (benzyl phenyl sulfide) showed less conversion and percentage yield presumably due to the bulky nature of substrates which in turn hindered the ease of pore channel and active vanadium sites. The turnover frequency values for differently substituted sulphoxides in the presence of catalyst were further compared (Table S1c). Moreover, the oxidation of methylphenyl sulfide was also performed using 30% H₂O₂ as oxidizing agent, which led to 68% conversion after 4 h at ambient temperature. The GC-MS data of dimethyl sulfoxide, methylphenyl sulfoxide, and benzyl phenyl sulfoxide are shown in Figures S19–S23.

The possible mechanism of sulfide oxidation is illustrated in Figure 4, first, the active vanadium moieties of VO-TAPT-2,3-DHTA coordinated with the oxygen atom of TBHP thereby promoting the formation of oxygenated intermediate. Second, the intermediate undergoes nucleophilic attack on the sulfide followed by concerted oxygen transfer led to sulfoxide with the regeneration of catalyst. The heterogeneity of VO-TAPT-2,3-DHTA was testified by leaching experiments for

Table 3. Sulfide Oxidation with Differently Substituted Substrates Catalyzed with VO-TAPT-2,3-DHTA COF and Other Homogenous Analogue^a

| Entry | Sulphide | Sulphoxide | Time (h) | % Conversion | % Yield |
|----------------|---|---|----------|--------------|---------|
| 1 |  |  | 4 | 99 | 96 |
| 2 |  |  | 4 | 99 | 95 |
| 3 ^b |  |  | 4 | 84 | 75 |
| 4 ^c |  |  | 4 | 93 | 81 |
| 5 |  |  | 4 | 96 | 92 |
| 6 |  |  | 4 | 97 | 93 |
| 7 |  |  | 4 | 88 | 82 |

^aReaction condition: sulfide (1 mmol); TBHP (1.5 mmol); catalyst: 20 mg, containing 0.019 mmol of vanadium; CH₃CN = 3 mL; 25 °C; 100 rpm; 4 h. ^bReaction was carried out using VO(acac)₂ (4 mol%). ^cReaction was performed using VO(catechol)₂ (4 mol%).

both catalytic reactions. In a typical procedure, VO-TAPT-2,3-DHTA was filtered keeping the filtrate under the same condition, no change in conversion and percentage yield was observed for Prins reaction and sulfide oxidation. These observations underlining the profound role of catalyst and confirming the heterogeneity (Figures S24–S25). In addition, we performed control experiments for both catalytic reactions. The Prins reaction and sulfide oxidation were catalyzed by VO-TAPT-2,3-DHTA COF with vanadium concentration from 0.005 to 0.025 mmol for latter and 0.6 mmol for former, as shown in Table S2a. Notably, the increase in catalyst loading positively facilitates the conversion of sulfide to sulphoxide and percentage yield of nopol. Moreover, 1 mmol of dimethylsulfide reacted with varying amount of TBHP (0.25–2.0 mmol) led to conversion from 70 to 99%. The optimization concentration would be ≥ 1 mmol for TBHP with 99% conversion and 99% sulphoxide selectivity indicating pseudo first-order reaction (Table S1). Similar observation was also observed for Prins reaction with varying amounts of paraformaldehyde and vanadium loading of catalyst, as shown in Table S2.

Catalyst recyclability and long-lasting stability are key essential features of any catalysts to be considered for potential use in a large-scale industrial application. In this regard, the catalyst was recovered by filtration after the catalytic reactions followed by extensive wash with copious amounts of tetrahydrofuran, acetone before using for next catalytic reaction. The percentage yields of nopol and methylphenyl sulfoxide after third catalytic cycle are still impressive, as shown in Figure 5, thereby implying the excellent recyclability of vanadium-docked framework. The recovered catalyst was exposed to physicochemical analysis such as PXRD, FT-IR, and SEM to verify excellent stability of framework. The well-preserved PXRD and FT-IR profiles of VO-TAPT-2,3-DHTA after third catalytic cycle in both catalytic reactions indicating retainment of crystallinity, imine, and V=O functionalities ($C=N = 1620\text{ cm}^{-1}$ and $V=O = 970\text{ cm}^{-1}$), as shown in Figures S26–S29. Moreover, SEM and EDS mapping via SEM of the recycled VO-TAPT-2,3-DHTA COF showed well-defined petal-like morphology along with the uniform distributions of C, N, O, and V elements same as pristine framework (Figure S30). These results in accumu-

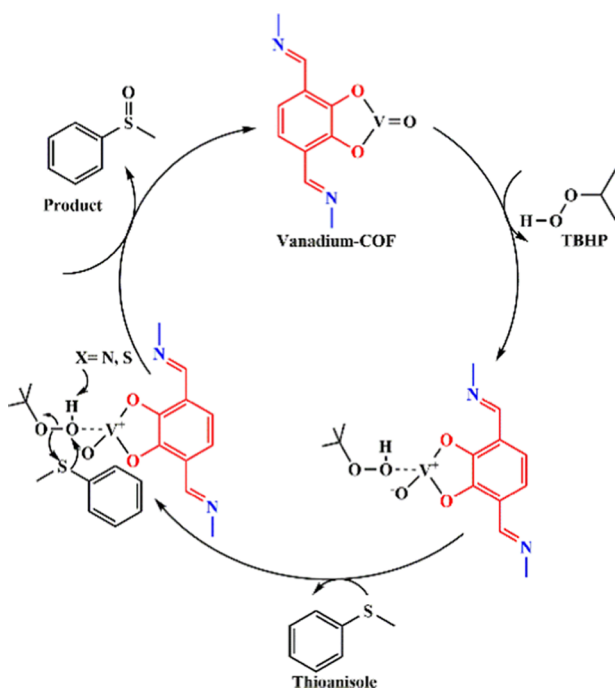


Figure 4. Proposed catalytic mechanism of VO-TAPT-2,3-DHTA COF-catalyzed sulfide oxidation.

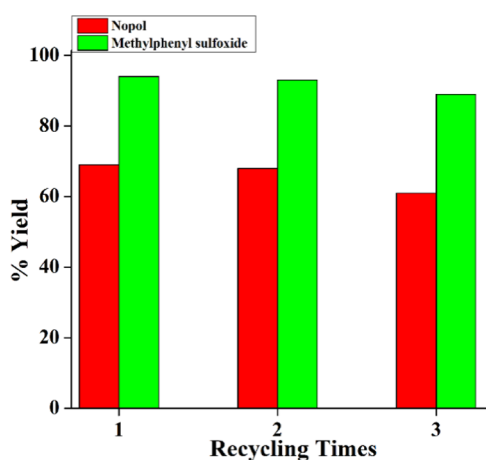


Figure 5. Recycling test of VO-TAPT-2,3-DHTA COF for Prins reaction and sulfide oxidation.

lation emphasize the importance of docking transition metals in COFs for pivotal organic reactions with complete retention of framework crystallinity up to three catalytic cycles. To further claim the stability of recyclable VO-TAPT-2,3-DHTA framework, we compared the surface area, XPS spectrum, ICP-MS, and Raman spectrum with pristine VO-TAPT-2,3-DHTA catalyst, and no drastic change was observed, as shown in Figures S31–S33. Additionally, dynamic light scattering (DLS) measurements were performed to determine the possible formation of nanoparticles during the catalytic reactions. We performed the experiment under appropriate reaction condition in the presence and absence of catalyst and compared the particle size of the filtrate (Figure S34), which showed no extra peak, thereby discarding the possibility of nanoparticle aggregation. Our work not only contributes docking of transition metals in porous materials for catalytic applications but also opens the door of different

functionalizations in COFs for various applications from greenhouse gases adsorption to water purification.

CONCLUSIONS

In summary, we have successfully synthesized and explored the profound role of vanadium-docked framework, VO-TAPT-2,3-DHTA, as an effective and efficient heterogeneous catalyst for key organic reactions, namely, Prins reaction and sulfide oxidation. The vanadium coordination with the O,O moieties in the pores of mesoporous framework showing high surface area exhibited an excellent catalytic activity for nopol synthesis and range of sulfides oxidation without any losses of structural integrity, stability, and activity for many times. We believe that such a strategy can be extended to other high-valent transition-metal ions such as niobium and other frameworks bearing N,N moieties and metallic systems such as Pd, Ir, Rh in catalyzing various other pivotal organic and organometallic reactions. Research along this line is currently undergoing in our laboratory.

ASSOCIATED CONTENT

Supporting Information

The Supporting Information is available free of charge on the ACS Publications website at DOI: 10.1021/acsami.8b19352.

¹H NMR of amine; aldehyde precursors (Figure S1); PXRD pattern comparison of TAPT-2,3-DHTA COF with simulated pattern (Figure S2); FT-IR spectrum of TAPT-2,3-DHTA COF (Figure S3); TGA plot of TAPT-2,3-DHTA COF (Figure S4); VT-PXRD of TAPT-2,3-DHTA COF (Figure S5); ¹³C NMR of TAPT-2,3-DHTA COF (Figure S6); pore size distribution of TAPT-2,3-DHTA COF (Figure S7); CO₂ adsorption isotherm of TAPT-2,3-DHTA COF (Figure S8); FT-IR spectrum of VO-TAPT-2,3-DHTA COF (Figure S9); TGA plot of VO-TAPT-2,3-DHTA COF (Figure S10); VT-PXRD of VO-TAPT-2,3-DHTA COF (Figure S11); DLS measurement of VO-TAPT-2,3-DHTA COF (Figure S12); pore size distribution of VO-TAPT-2,3-DHTA COF (Figure S13); CO₂ adsorption isotherm of VO-TAPT-2,3-DHTA COF (Figure S14); ¹³C NMR of VO-TAPT-2,3-DHTA COF (Figure S15); Raman spectra of TAPT-2,3-DHTA and VO-TAPT-2,3-DHTA COFs (Figure S16); PXRD pattern of VO-TAPT-2,3-DHTA COF in CH₃CN (Figure S17); FT-IR spectrum of VO-TAPT-2,3-DHTA COF in CH₃CN (Figure S18); GC-MS data of nopol, methylphenyl sulphoxide, dimethyl sulphoxide, benzyl phenyl sulphoxide, dimethyl sulfone (Figures S19–S23); effect of reaction condition on Prins reaction and sulfide oxidation (Tables S1 and S2); leaching test for Prins reaction and sulfide oxidation (Figures S24–S25); PXRD pattern comparison of VO-TAPT-2,3-DHTA COF before and after catalytic reactions (Figures S26 and S28); FT-IR spectrum comparison of VO-TAPT-2,3-DHTA COF before and after catalytic reactions (Figures S27 and S29); SEM and EDS mapping of VO-TAPT-2,3-DHTA COF after catalysis (Figure S30); comparison of surface area before and after catalysis (Figure S31); XPS spectra of VO-TAPT-2,3-DHTA COF after catalysis (Figure S32); Raman spectra comparison of VO-TAPT-2,3-DHTA COF before

and after catalysis (Figure S33); particle size distribution with and without catalyst (Figure S34); elemental analysis of TAPT-2,3-DHTA and VO-TAPT-2,3-DHTA COFs (Table S3); comparison among various heterogeneous catalysts for Nopol synthesis (Table S4); fractional atomic coordinate of VO-TAPT-2,3-DHTA COF (Table S5) (PDF)

AUTHOR INFORMATION

Corresponding Author

*E-mail: sqma@usf.edu.

ORCID

Swetha Ramani: 0000-0003-1850-6635

Zhongyu Yang: 0000-0002-3018-3608

Shengqian Ma: 0000-0002-1897-7069

Notes

The authors declare no competing financial interest.

ACKNOWLEDGMENTS

The authors acknowledge University of South Florida (USF) for support of this work. The authors also extend their sincere appreciation to the Deanship of Scientific Research at King Saud University for partially funding this Research Group (RG-1435-010). The authors thank Prof. Humberto R. Gutiérrez for helping with the Raman experiments.

REFERENCES

- Jin, Y.; Hu, Y.; Zhang, W. Tessellated Multiporous Two-Dimensional Covalent Organic Frameworks. *Nat. Rev. Chem.* **2017**, *1*, No. 0056.
- Feng, X.; Ding, X.; Jiang, D. Covalent Organic Frameworks. *Chem. Soc. Rev.* **2012**, *41*, 6010–6022.
- Ding, S.-Y.; Wang, W. Covalent Organic Frameworks (COFs): from Design to Applications. *Chem. Soc. Rev.* **2013**, *42*, 548–568.
- Bisbey, R. P.; Dichtel, W. R. Covalent Organic Frameworks as a Platform for Multidimensional Polymerization. *ACS Cent. Sci.* **2017**, *3*, 533–543.
- Beuerle, F.; Gole, B. Covalent Organic Frameworks and Cage Compounds: Design and Applications of Polymeric and Discrete Organic Scaffolds. *Angew. Chem., Int. Ed.* **2018**, *57*, 4850–4878.
- Diercks, C. S.; Yaghi, O. M. The Atom, the Molecule, and the Covalent Organic Framework. *Science* **2017**, *355*, No. eaal1585.
- Slater, A. G.; Cooper, A. I. Function-led Design of New Porous Materials. *Science* **2015**, *348*, 988–998.
- Waller, P. J.; Gandara, F.; Yaghi, O. M. Chemistry of Covalent Organic Frameworks. *Acc. Chem. Res.* **2015**, *48*, 3053–3063.
- Huang, N.; Wang, P.; Jiang, D. Covalent organic frameworks: a Materials Platform for Structural and Functional Design. *Nat. Rev. Mater.* **2016**, *1*, No. 16068.
- Song, Y.; Sun, Q.; Aguila, B.; Ma, S. Opportunities of Covalent Organic Frameworks for Advanced Applications. *Adv. Sci.* **2018**, *417*, No. 1801410.
- Lohse, M. S.; Bein, T. Covalent Organic Frameworks: Structure, Synthesis and Applications. *Adv. Funct. Mater.* **2018**, *28*, No. 1705553.
- Côté, A. P.; Benin, A. I.; Ockwig, N. W.; Ó'Keeffe, M.; Matzger, A. J.; Yaghi, O. M. Porous, Crystalline, Covalent Organic Frameworks. *Science* **2005**, *310*, 1166–1170.
- Pang, Z.-F.; Xu, S.-Q.; Zhou, T.-Y.; Liang, R.-R.; Zhan, T.-G.; Zhao, X. Construction of Covalent Organic Frameworks Bearing Three Different Kinds of Pores through the Heterostructural Mixed Linker Strategy. *J. Am. Chem. Soc.* **2016**, *138*, 4710–4713.
- Kandambeth, S.; Mallick, A.; Lukose, B.; Mane, M. V.; Heine, T.; Banerjee, R. Construction of Crystalline 2D Covalent Organic Frameworks with Remarkable Chemical (Acid/Base) Stability via a Combined Reversible and Irreversible Route. *J. Am. Chem. Soc.* **2012**, *134*, 19524–19527.
- Uribe-Romo, F. J.; Doonan, C. J.; Furukawa, H.; Oisaki, K.; Yaghi, O. M. Crystalline Covalent Organic Frameworks with Hydrazone Linkage. *J. Am. Chem. Soc.* **2011**, *133*, 11478–11481.
- Ma, T.; Kapustin, E. A.; Yin, S. X.; Liang, L.; Zhou, Z.; Niu, J.; Li, H.; Wang, Y.; Su, J.; Li, J.; Wang, X.; Wang, W. D.; Wang, W.; Sun, J.; Yaghi, O. M. Single Crystal X-ray Diffraction Structure of Covalent Organic Frameworks. *Science* **2018**, *361*, 48–52.
- Du, Y.; Yang, H.; Whiteley, J. M.; Wan, S.; Jin, Y.; Lee, S.-H.; Zhang, W. Ionic Covalent Organic Frameworks with Spiroborate Linkage. *Angew. Chem., Int. Ed.* **2016**, *55*, 1737–1741.
- Doonan, C. J.; Tranchemontagne, D. J.; Glover, T. G.; Hunt, J. R.; Yaghi, O. M. Exceptional Ammonia Uptake by a Covalent Organic Framework. *Nat. Chem.* **2010**, *2*, 235–238.
- Zeng, Y.; Zou, R.; Zhao, Y. Covalent Organic Frameworks for CO₂ Capture. *Adv. Mater.* **2016**, *28*, 2855–2873.
- Baldwin, L. A.; Crowe, J. W.; Pyles, D. A.; McGrier, P. L. Metalation of a Mesoporous Three-Dimensional Covalent Organic Framework. *J. Am. Chem. Soc.* **2016**, *138*, 15134–15137.
- Pramudya, Y.; Mendoza-Cortes, J. L. Design Principles for High H₂ Storage using Chelation of Abundant Transition Metals in Covalent Organic Frameworks for 0–700 bar at 298 K. *J. Am. Chem. Soc.* **2016**, *138*, 15204–15213.
- Yang, Y.; Faheem, M.; Wang, L.; Meng, Q.; Sha, H.; Yang, N.; Yuan, Y.; Zhu, G. Surface Pore Engineering of Covalent Organic Frameworks for Ammonia Capture through Synergistic Multivariate and Open Metal Site Approached. *ACS Cent. Sci.* **2018**, *4*, 748–754.
- Zhang, J.; Han, X.; Wu, X.; Liu, Y.; Cui, Y. Multivariate Chiral Covalent Organic Frameworks with Controlled Crystallinity and Stability for Asymmetric Catalysis. *J. Am. Chem. Soc.* **2017**, *139*, 8277–8285.
- Banerjee, T.; Haase, F.; Savasci, G.; Gottschling, K.; Ochsenfeld, C.; Lotsch, B. V. Single-site Photocatalytic H₂ Evolution from Covalent Organic Frameworks with Molecular Cobaloxime-Cocatalysts. *J. Am. Chem. Soc.* **2017**, *139*, 16228–16234.
- Lu, S.; Hu, Y.; Wan, S.; McCaffrey, R.; Jin, Y.; Gu, H.; Zhang, W. Synthesis of Ultrafine and Highly Dispersed Metal Nanoparticles Confined in a Thioether-Containing Covalent Organic Framework and Their Catalytic Application. *J. Am. Chem. Soc.* **2017**, *139*, 17082–17088.
- Diercks, C. S.; Lin, S.; Kornienko, N.; Kapustin, E. A.; Nichols, E. M.; Zhu, C.; Zhao, Y.; Chang, C. J.; Yaghi, O. M. Reticular Electronic Tuning of Porphyrin Active Sites in Covalent Organic Frameworks for Electrocatalytic Carbon Dioxide Reduction. *J. Am. Chem. Soc.* **2018**, *140*, 1116–1122.
- Han, X.; Xia, Q.; Huang, J.; Liu, Y.; Tan, C.; Cui, Y. Chiral Covalent Organic Frameworks with High Chemical Stability for Heterogeneous Asymmetric Catalysis. *J. Am. Chem. Soc.* **2017**, *139*, 8693–8697.
- Pachfule, P.; Acharjya, A.; Roeser, J.; Langenhahn, T.; Schwarze, M.; Schomacker, R.; Thomas, A.; Schmidt, J. Diacetylene Functionalized Covalent Organic Framework (COF) for Photocatalytic Hydrogen Generation. *J. Am. Chem. Soc.* **2018**, *140*, 1423–1427.
- Wei, P.-F.; Qi, M.-Z.; Wang, Z.-P.; Ding, S.-Y.; Yu, W.; Liu, Q.; Wang, L.-K.; Wang, H.-Z.; An, W.-K.; Wang, W. Benzoxazole-Linked Ultrastable Covalent Organic Frameworks for Photocatalysis. *J. Am. Chem. Soc.* **2018**, *140*, 4623–4631.
- Sick, T.; Hufnagel, A. G.; Kampmann, J.; Kondofersky, I.; Calik, M.; Rotter, J. M.; Evans, A.; Dobliger, M.; Herbert, S.; Peters, K.; Bohm, D.; Knochel, P.; Medina, D. D.; Fattakhova-Rohlfing, D.; Bein, T. Oriented Films of Conjugated 2D Covalent Organic Frameworks as Photocathodes for Water Splitting. *J. Am. Chem. Soc.* **2018**, *140*, 2085–2092.
- Lin, S.; Diercks, C. S.; Zhang, Y.-B.; Kornienko, N.; Nichols, E. M.; Zhao, Y.; Paris, A. R.; Kim, D.; Yang, P.; Yaghi, O. M.; Chang, C. J. Covalent Organic Frameworks Comprising Cobalt Porphyrins for Catalytic CO₂ Reduction in Water. *Science* **2015**, *349*, 1208–1213.

- (32) Ding, S.-Y.; Gao, J.; Wang, Q.; Zhang, Y.; Song, W.-G.; Su, C.-Y.; Wang, W. Construction of Covalent Organic Framework for Catalysis: Pd/COF-LZU 1 in Suzuki-Miyaura coupling reaction. *J. Am. Chem. Soc.* **2011**, *133*, 19816–19822.
- (33) Vyas, V. S.; Haase, F.; Stegbauer, L.; Savasci, G.; Podjaski, F.; Ochsenfeld, C.; Lotsch, B. V. A Tunable Azine Covalent Organic Framework Platform for Visible Light-Induced Hydrogen Generation. *Nat. Commun.* **2015**, *6*, No. 8508.
- (34) Sun, Q.; Aguila, B.; Perman, J. A.; Nguyen, N.; Ma, S. Flexibility Matters: Cooperation Active Sites in Covalent Organic Framework and Threaded Ionic Polymer. *J. Am. Chem. Soc.* **2016**, *138*, 15790–15796.
- (35) Wang, X.; Han, X.; Zhang, J.; Wu, X.; Liu, Y.; Cui, Y. Homochiral 2D Porous Covalent organic Frameworks for Heterogeneous Asymmetric Catalysis. *J. Am. Chem. Soc.* **2016**, *138*, 12332–12335.
- (36) Bertrand, G. H. V.; Michaelis, V. K.; Ong, T.-C.; Griffin, R. G.; Dincà, M. Thiophene-based Covalent Organic Frameworks. *Proc. Natl. Acad. Sci. U.S.A.* **2013**, *110*, 4923–4928.
- (37) Calik, M.; Auras, F.; Salonen, L. M.; Bader, K.; Grill, I.; Handloser, M.; Medina, D. D.; Dogru, M.; Löbermann, F.; Trauner, D.; Hartschuh, A.; Bein, T. Extraction of Photogenerated Electrons and Holes from a Covalent Organic Framework Integrated Heterojunction. *J. Am. Chem. Soc.* **2014**, *136*, 17802–17807.
- (38) Chen, L.; Furukawa, K.; Gao, J.; Nagai, A.; Nakamura, T.; Dong, Y.; Jiang, D. Photoelectric Covalent Organic Frameworks: Converting Open Lattices into Ordered Donor-Acceptor Heterojunctions. *J. Am. Chem. Soc.* **2014**, *136*, 9806–9809.
- (39) Sun, Q.; Aguila, B.; Perman, J.; Earl, L.; Abney, C.; Cheng, Y.; Wei, H.; Nguyen, N.; Wojtas, L.; Ma, S. Postsynthetically Modified Covalent Organic Frameworks for Efficient and Effective Mercury Removal. *J. Am. Chem. Soc.* **2017**, *139*, 2786–2793.
- (40) Sun, Q.; Aguila, B.; Earl, L. D.; Abney, C. W.; Wojtas, L.; Thallpally, P. K.; Ma, S. Covalent Organic Frameworks as a Decorating Platform for Utilization and Affinity Enhancement of Chelating Sites for Radionuclide Sequestration. *Adv. Mater.* **2018**, *30*, No. 1705479.
- (41) Fang, Q.; Wang, J.; Gu, S.; Kaspar, R. B.; Zhuang, Z.; Zheng, J.; Guo, H.; Qiu, S.; Yan, Y. 3D Porous Crystalline Polyimide Covalent Organic Frameworks for Drug Delivery. *J. Am. Chem. Soc.* **2015**, *137*, 8352–8355.
- (42) Kandambeth, S.; Venkatesh, V.; Shinde, D. B.; Kumari, S.; Halder, A.; Verma, S.; Banerjee, R. Self-templated Chemically Stable Hollow Spherical Covalent Organic Framework. *Nat. Commun.* **2015**, *6*, No. 6786.
- (43) Wang, S.; Wang, Q.; Shao, P.; Han, Y.; Gao, X.; Ma, L.; Yuan, S.; Ma, X.; Zhou, J.; Feng, X.; Wang, B. Exfoliation of Covalent Organic Frameworks into Few-Layer Redox-Active Nanosheets as Cathode Materials for Lithium-Ion Batteries. *J. Am. Chem. Soc.* **2017**, *139*, 4258–4261.
- (44) Ning, G.-H.; Chen, Z.; Gao, Q.; Tang, W.; Chen, Z.; Liu, C.; Tian, B.; Li, X.; Loh, K. P. Salicylideneanilines-Based Covalent Organic Frameworks as Chemoselective Molecular Sieves. *J. Am. Chem. Soc.* **2017**, *139*, 8897–8904.
- (45) Peng, Y.; Huang, Y.; Zhu, Y.; Chen, B.; Wang, L.; Lai, Z.; Zhang, Z.; Zhao, M.; Tan, C.; Yang, N.; Shao, F.; Han, Y.; Zhang, H. Ultrathin Two-Dimensional Covalent Organic framework Nanosheets: Preparation and Application in Highly Sensitive and Selective DNA Detection. *J. Am. Chem. Soc.* **2017**, *139*, 8698–8704.
- (46) Sun, Q.; Aguila, B.; Perman, J.; Butts, T.; Xiao, F.-S.; Ma, S. Imparting Superwettability within Covalent Organic Frameworks for Functional Coating. *Chem* **2018**, *4*, 1726–1739.
- (47) Han, X.; Huang, J.; Yuan, C.; Liu, Y.; Cui, J. Chiral 3D Covalent Organic Frameworks for High Performance Liquid Chromatographic Enantioseparation. *J. Am. Chem. Soc.* **2018**, *140*, 892–895.
- (48) Mitra, S.; Sasmal, H. S.; Kundu, T.; Kandambeth, S.; Illath, K.; Daiz, D. D.; Banerjee, R. Targeted Drug Delivery in Covalent Organic Nanosheets (CONs) via Sequential Postsynthetic Modification. *J. Am. Chem. Soc.* **2017**, *139*, 4513–4520.
- (49) Zhang, S.; Zheng, Y.; An, H.; Aguila, B.; Yang, C.-X.; Dong, Y.; Xie, W.; Cheng, P.; Zhang, Z.; Chen, Y.; Ma, S. Covalent Organic Frameworks with Chirality Enriched by Biomolecules for Efficient Chiral Separation. *Angew. Chem., Int. Ed.* **2018**, *57*, 16754–16759.
- (50) Lin, C.-Y.; Zhang, D.; Zhao, Z.; Xia, Z. Covalent Organic Framework Electrocatalysts for Clean Energy Conversion. *Adv. Mater.* **2018**, *30*, No. 1703646.
- (51) Langeslay, R. R.; Kaphan, D. M.; Marshall, C. L.; Stair, P. C.; Sattelberger, A. P.; Delferro, M. Catalytic Application of Vanadium: A Mechanistic Perspective. *Chem. Rev.* **2018**, DOI: 10.1021/acs.chemrev.8b00245.
- (52) Dickman, M. H.; Pope, M. T. Peroxo and Superoxo Complexes of Chromium, Molybdenum, and Tungsten. *Chem. Rev.* **1994**, *94*, 569–584.
- (53) Halder, A.; Kandambeth, S.; Biswal, B. P.; Gaur, G.; Roy, N. C.; Addicoat, M.; Salunke, J. K.; Banerjee, S.; Vanka, K.; Heine, T.; Verma, S.; Banerjee, R. Decoding the Morphological Diversity in Two Dimensional Crystalline Porous Polymers by Core Planarity Modulation. *Angew. Chem., Int. Ed.* **2016**, *55*, 7806–7810.
- (54) Bledsoe, J. O. *Kirk-Othmer Encyclopedia of Chemical Technology*. Kroschwitz, J. I.; Howe-Grant, M., Eds.; Wiley: New York, 1997; Vol. 23, pp 833.
- (55) *Common Fragrance and Flavor Materials, Preparation, Properties, and Uses*; Surburg, H.; Panten, J., Eds.; Wiley-VCH: Weinheim, 2006; pp 67–68.
- (56) Bain, J. P. Nopol. I. Reaction of β -Pinene with Formaldehyde. *J. Am. Chem. Soc.* **1946**, *68*, 638–641.
- (57) Minh Do, D.; Jaenicke, S.; Chuah, G.-K. Mesoporous Zr-SBA-15 as a Green Solid Acid Catalyst for the Prins Reaction. *Catal. Sci. Technol.* **2012**, *2*, 1417–1424.
- (58) de Villa, A. L. P.; Alarcon, E.; Montes de Correa, C. Synthesis of Nopol over MCM-41 Catalysts. *Chem. Commun.* **2002**, *68*, 2654–2655.
- (59) Alarcón, E. A.; De Villa, A. L. P.; Montes de Correa, C. Characterization of Sn- and Zn-Loaded MCM-41 Catalysts for Nopol Synthesis. *Microporous Mesoporous Mater.* **2009**, *122*, 208–215.
- (60) Kubeč, R.; Svobodová, M.; Velišek, J. Distribution of S-Alk(en)ylcysteine Sulfoxides in some Allium species. Identification of a New Flavor Precursor: S-Ethylcysteine Sulfoxide (Ethiin). *J. Agric. Food Chem.* **2000**, *48*, 428–433.
- (61) Frenzel, R.; Sathicq, A. G.; Blanco, M. N.; Romanelli, G. P.; Pizzio, L. R. Carbon-Supported Metal-modified Lacunary Tungstosilicic Polyoxometallates used as Catalysts in the Selective Oxidation of Sulphides. *J. Mol. Catal. A: Chem.* **2015**, *403*, 27–36.
- (62) Jalilian, F.; Yadollahi, B.; Riahi Farsani, M.; Tangestaninejad, S.; Rudbari, H. A.; Habibi, R. New Perspective to Keplerate polyoxomolybdates: Green Oxidation of Sulfides with Hydrogen Peroxide in Water. *Catal. Commun.* **2015**, *66*, 107–110.
- (63) Gomes, R.; Bhanja, P.; Bhaumik, A. A Triazine-based Covalent Organic Polymer for Efficient CO₂ Adsorption. *Chem. Commun.* **2015**, *51*, 10050–10053.
- (64) Grudzień, K.; Malinska, M.; Barbasiewicz, M. Synthesis and Properties of Bimetallic Hoveyda-Grubbs Metathesis Catalysts. *Organometallics* **2012**, *31*, 3636–3646.
- (65) Cooper, S. R.; Koh, Y. B.; Raymond, K. N. Synthesis, Structural, and Physical Studies of Bis(triethylammonium)Tris(catecholato)-vanadate(IV), Potassium Bis(catcholato)oxovanadate(IV), and Potassium Tris(catecholato)vanadate(III). *J. Am. Chem. Soc.* **1982**, *104*, 5092–5102.
- (66) Sun, Q.; Fu, C.-W.; Aguila, B.; Perman, J.; Wang, S.; Huang, H.-Y.; Xiao, F.-S.; Ma, S. Pore Environment Control and Enhanced Performance of Enzymes Infiltrated in Covalent Organic Frameworks. *J. Am. Chem. Soc.* **2018**, *140*, 984–992.
- (67) Lu, Q.; Ma, Y.; Li, H.; Guan, X.; Yusran, Y.; Xue, M.; Fang, Q.; Yan, Y.; Qiu, S.; Valtchev, V. Postsynthetic Functionalization of Three-Dimensional Covalent Organic Frameworks for Selective

Extraction of Lanthanide Ions. *Angew. Chem., Int. Ed.* **2018**, *57*, 6042–6048.

(68) Leng, W.; Peng, Y.; Zhang, J.; Lu, H.; Xiao, F.; Ge, R.; Dong, B.; Wang, B.; Hu, X.; Gao, Y. Sophisticated Design of Covalent Organic Frameworks with Controllable Bimetallic Docking for a Cascade Reaction. *Chem. - Eur. J.* **2016**, *22*, 9087–9091.

(69) Baltes, M.; Van Der Voort, P.; Weckhuysen, B. M.; Ramachandra Rao, R.; Catana, G.; Schoonheydt, R. A.; Vansant, E. F. Synthesis and characterization of alumina-supported vanadium oxide catalysts prepared by the molecular designed dispersion of VO(acac)₂ complexes. *Phys. Chem. Chem. Phys.* **2000**, *2*, 2673–2680.

(70) Maurya, M. R.; Kumar, U.; Manikandan, P. Polymer Supported Vanadium and Molybdenum Complexes as Potential Catalysts for the Oxidation and Oxidative Bromination of Organic Substrates. *Dalton Trans.* **2006**, *187*, 3561–3575.